ChemComm

COMMUNICATION

View Article Online
View Journal | View Issue

Cite this: *Chem. Commun.*, 2025, **61**, 3191

Received 5th October 2024,
Accepted 9th December 2024

DOI: 10.1039/d4cc05132g

rsc.li/chemcomm

Interfacial engineering-induced electronic state modulation in Ru/MoS_2 heterostructures for efficient hydrogen evolution reaction†

Ning Wang,‡[abcd] Yajing Zhang,‡[bcde] Canhui Zhang,[abcd] Xingkun Wang,[bcd] Shuixing Dai,[abc] Minghua Huang *[a] and Heqing Jiang *[bcd]

In traditional binary heterojunction catalysts, mismatched energy band structures lead to higher electron transfer barriers. By reducing the work function difference *via* a ternary Ru–RuS_2/MoS_2 heterostructure, we developed a HER catalyst with remarkable activity (17 mV@10 mA cm^{-2}) and excellent stability (300 h@500 mA cm^{-2}).

Alkaline water electrolysis serves as an efficient method for hydrogen production. The development of efficient and durable electrocatalysts to improve the kinetics of the hydrogen evolution reaction (HER) is essential for the large-scale production of green hydrogen.[1] To date, Pt-based catalysts are effective but limited by high cost and scarcity.[2] MoS_2, with its active metallic edges, is a promising Pt alternative for HER.[3] Nevertheless, the application of MoS_2 as a catalyst in HER is restricted by its limited density of active sites and poor electrical conductivity.[4]

Strategies like phase engineering,[5] defect engineering,[6] doping,[7] and heterostructure construction[8] have been explored. Among these approaches, metal (such as Pb, Ru, Co, *etc.*) doping has been extensively validated as an effective strategy to significantly enhance the HER catalytic activity of MoS_2. As one of the most cost-effective noble metals, Ru has demonstrated significant advantages in the field of water splitting.[9,10] However, direct contact between metals and wide-bandgap semiconductors often introduces significant impedance. In recent years, the effective design and construction of heterostructures have been demonstrated to facilitate the directional transport of electrons as a solution to this issue. For example, Huang *et al.* developed a metallic heterostructure, Mo_2S_3@$NiMo_3S_4$, with excellent electron transfer, fast reaction kinetics, and strong structural stability, achieving overpotentials of 173 mV for OER and 32 mV for HER at 10 mA cm^{-2}.[9] Nonetheless, the work function disparity between metallic nanoparticles and MoS_2 obstructs electron transfer, leading to increased energy losses and reduced catalytic efficiency. Although some studies have attempted to address this challenge, further exploration of effective strategies is still required to enhance catalytic performance.

Herein, we constructed a Ru–RuS_2/MoS_2 heterostructure, where RuS_2 serves as a "cross-interfacial electron bridge" between narrow-bandgap Ru and wide-bandgap MoS_2. This interfacial design reduces ohmic impedance and enhances electron transfer. Ru–RuS_2/MoS_2 delivers outstanding HER performance with a low overpotential of 17 mV (10 mA cm^{-2}) and stability for over 300 h (500 mA cm^{-2}). Density functional theory (DFT) results indicate that the incorporation of RuS_2 reduces the bandgap of Ru–MoS_2, facilitates the directional transfer of electrons from Ru sites to MoS_2, and lowers the dissociation energy of $*H_2O$ as well as the adsorption energy of *H. This simultaneously enhances water dissociation and hydrogen desorption, thereby significantly accelerating the HER process.

As depicted in Fig. 1a, the synthesis of Ru–RuS_2/MoS_2 follows a four-step process (Experimental Section for details ESI†). The Ru–MoS_2 was synthesized by the same method. The XRD pattern of Ru–RuS_2/MoS_2 (Fig. 1b) reveals characteristic peaks at 27.519°, 31.881°, 45.710°, and 54.186°, corresponding to the (111), (200), (220), and (311) planes of RuS_2 (PDF#97-004-1996). Additionally, peaks at 14.125°, 32.911°, 39.512°, and 58.764° are associated with the (002), (100), (103), and (110) planes of MoS_2 (PDF#97-003-1067). These observations preliminarily indicate the formation of a RuS_2/MoS_2 heterojunction structure in Ru–RuS_2/MoS_2. Furthermore, Raman spectroscopy was conducted on MoS_2, Ru–MoS_2, and Ru–RuS_2/MoS_2 samples (Fig. S1, ESI†). Raman spectroscopy analysis demonstrated that, in addition to the A_{1g} and E^1_{2g} modes of MoS_2, the Ru–RuS_2/MoS_2 exhibited a

[a] *Ocean University of China, Qingdao 266100, China. E-mail: huangminghua@ouc.edu.cn*
[b] *Key Laboratory of Functional Membrane Material and Membrane Technology, Qingdao Institute of Bioenergy and Bioprocess Technology, Chinese Academy of Sciences, 189 Songling Road, Qingdao, 266101, China. E-mail: jianghq@qibebt.ac.cn*
[c] *Shandong Energy Institute, Qingdao, 266101, China*
[d] *Qingdao New Energy Shandong Laboratory, Qingdao, 266101, China*
[e] *University of Chinese Academy of Sciences, Beijing 100049, China*

† Electronic supplementary information (ESI) available: Experimental procedures; catalyst characterization. See DOI: https://doi.org/10.1039/d4cc05132g

‡ These authors contributed equally to this work.

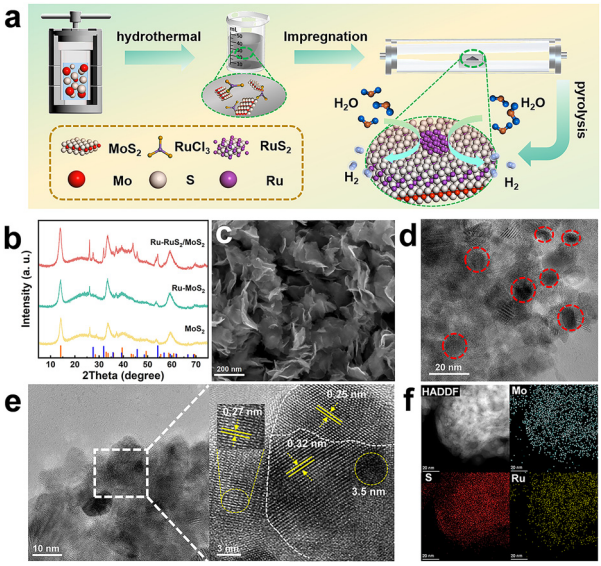

Fig. 1 Characterization of the structure and morphology of catalysts. (a) The synthesis process schematic diagram of Ru–RuS_2/MoS_2; (b) XRD pattern of MoS_2, Ru–MoS_2 and Ru–RuS_2/MoS_2; (c) SEM image; (d) TEM image, (e) HRTEM (inset high-magnified HRTEM image) and (f) elemental mapping images of Mo, S, Ru for the Ru–RuS_2/MoS_2.

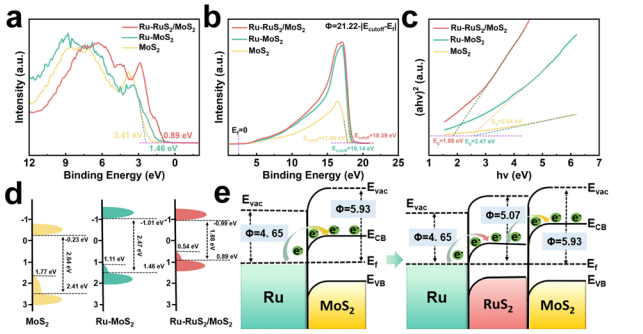

Fig. 2 Characterization of valence states and electronic structure. (a) VB-XPS spectra, (b) UPS spectra and (c) UV-VIS spectra of MoS_2, Ru–MoS_2 and Ru–RuS_2/MoS_2; (d) energy band diagram of MoS_2, Ru–MoS_2 and Ru–RuS_2/MoS_2; (e) schematic diagram of band structures (E_f = Fermi level, E_{vac} = vacuum energy).

weak peak at 386 cm^{-1}, corresponding to RuS_2.[11] This observation further confirms the formation of RuS_2 structures in the target sample. SEM (Fig. 1c) shows a nanoflower-like structure in Ru–RuS_2/MoS_2, enhancing stability and active site density for better catalysis.[12] Moreover, SEM images at higher magnifications (Fig. S3, ESI†) reveal spherical structures attached to the nanoflowers, which preliminarily confirm the successful formation of Ru nanoclusters. TEM images reveal that Ru–RuS_2/MoS_2 exhibits a sheet-like distribution. Lattice fringes indicate the stacking of distinct nanosheets. Additionally, dark spots, which are uniformly distributed throughout the material, confirm the presence of Ru nanoclusters (Fig. 1d). The structure suggests a MoS_2–RuS_2 heterojunction with uniform Ru nanoclusters. To further investigate the nanostructure of Ru–RuS_2/MoS_2, high-resolution transmission electron microscopy (HRTEM) was employed for detailed analysis (Fig. 1e). In the magnified HRTEM images, lattice fringes with interplanar spacings of 0.25 nm, 0.27 nm, and 0.32 nm are observed, which correspond to the (102) and (100) planes of MoS_2 and the (111) plane of RuS_2, respectively. The results support the aforementioned hypothesis and confirm the successful formation of the heterointerfaces. In addition, high-angle annular dark field scanning transmission electron microscopy (HAADF-STEM) and corresponding elemental mapping uncover the homogeneous distribution of Mo, S, and Ru elements within the Ru–RuS_2/MoS_2 heterostructure (Fig. 1f). AFM (Fig. S4, ESI†) shows a consistent MoS_2 layered structure (~3.5 nm thickness) in all samples.

XPS was used to analyze electronic properties and valence states (Fig. S5, ESI†). The results indicate that the formation of RuS_2 induces a higher oxidation state of Ru in Ru–RuS_2/MoS_2.[13] Meanwhile, the electron transfer from the Ru nanoclusters to MoS_2 is also evidenced.[14] Moreover, the characteristic peaks of Ru^0 $3p_{1/2}$ (484.4 eV) and Ru^0 $3p_{3/2}$ (462.2 eV) reflect the presence of Ru nanoclusters. It is well established that the electrical conductivity of semiconductors is determined by the band gap within their energy band structure, with the transition of electrons between the valence band and the conduction band dictating their conductive properties.[15] To further investigate the impact of RuS_2 on electron conduction, we initially employed X-ray photoelectron spectroscopy valence band (VB-XPS) to analyze the VB positions of MoS_2, Ru–MoS_2, and Ru–RuS_2/MoS_2 (Fig. 2a). In contrast to MoS_2 (2.41 eV) and Ru–MoS_2 (1.46 eV), the valence band position of Ru–RuS_2/MoS_2 (0.89 eV) is significantly closer to the Fermi level. The lower valence band position confirms RuS_2's role as a "cross-interfacial electron bridge" optimizing the catalyst's electronic structure. To examine the effect of work function difference ($\Delta\Phi$) on electron transfer,[16] UPS was employed to determine the (Φ) values of MoS_2, Ru–MoS_2, and Ru–RuS_2/MoS_2. The corresponding results reveal that compared to the higher work function (Φ) values for MoS_2 (3.32 eV) and Ru–MoS_2 (3.08 eV), the Ru–RuS_2/MoS_2 possesses the lowest Φ value of 2.83 eV. A lower work function indicates a reduced energy requirement for electron emission, which in turn lowers the energy barrier, facilitates charge transfer, and enhances conductivity.[17] Simultaneously, UV-VIS analysis reveals the smallest band gap (1.88 eV) for Ru–RuS_2/MoS_2, supporting its high conductivity (Fig. 2c). This further corroborates the enhanced conductivity of Ru–RuS_2/MoS_2. DFT calculations also determine that the work function (Φ) of RuS_2 is 5.07 eV, which is lower than that of MoS_2 (Φ = 5.93 eV) but higher than that of Ru (Φ = 4.65 eV) (Fig. S6, ESI†). This satisfies the prerequisite for the formation of an interfacial energy barrier and supports the theoretical feasibility of RuS_2 acting as the "cross-interfacial electron bridge" to facilitate electron transfer from Ru to MoS_2 (Fig. 2d). After electronic modification, a significant optimization of the band structure was observed. The band diagrams of MoS_2, Ru–MoS_2, and Ru–RuS_2/MoS_2 were derived from VB-XPS and UV-VIS, as shown in Fig. 2e. Band diagrams reveal that RuS_2 shifts the valence band closer to the Fermi level and reduces the band gap, enhancing conductivity. The above findings demonstrate that

the introduction of RuS_2 effectively reduces the material's intrinsic ohmic impedance and enhances electron transfer from the metal to the wide-bandgap semiconductor.

We conducted electrochemical tests to verify the role of RuS_2 as a "cross-interfacial electron bridge" that enhances Ru to MoS_2 electron transfer and evaluated the catalytic HER performance of Ru–RuS_2/MoS_2. At a current density of 10 mA cm^{-2}, Ru–RuS_2/MoS_2 exhibited the lowest overpotential (η_{10} = 17 mV) (Fig. 3a and b and Fig. S7, ESI†), demonstrating its superior electron transfer capabilities. The heterostructure displayed a significantly lower Tafel slope of 75.9 mV dec^{-1} (Fig. 3c), indicating exceptional reaction kinetics. Moreover, the Tafel slope indicates that the Heyrovsky step is the rate-limiting process in HER.[18] We hypothesize that this phenomenon may be attributed to the heterostructure formed between MoS_2 and RuS_2, which facilitates electron transfer from Ru to the MoS_2 surface.

Additionally, Ru–RuS_2/MoS_2 has the highest electrochemical double-layer capacitance (C_{dl}) measurement of 19.99 mF cm^{-2} (Fig. 3d and Fig. S9, ESI†), and even after normalizing by the ECSA value, Ru–RuS_2/MoS_2 continues to show the highest current density (J_{ECSA}) (Fig. S10, ESI†), indicating it possesses a high density of active sites to participate in the HER process and rapid reaction kinetics. EIS reveals Ru–RuS_2/MoS_2 has the smallest semicircle (Fig. 3e), suggesting minimal charge transfer resistance.[19] Catalyst stability is essential for practical applications, which was appraised by chronopotentiometric test. As expected in Fig. 3f, the Ru–RuS_2/MoS_2 demonstrates stable operation for 300 h at 500 mA cm^{-2} in 1 M KOH, while still maintaining its morphology and structure (Fig. S11, ESI†). Meanwhile, the faraday efficiency of Ru–RuS_2/MoS_2 is 96.7%. Compared to most recently reported Ru-based and MoS_2-based catalysts, this catalyst exhibits the lowest overpotential (Fig. 3g and Table S1, ESI†). These results underscore that Ru–RuS_2/MoS_2 exhibits impressive HER activity and robust stability in alkaline electrolytes.

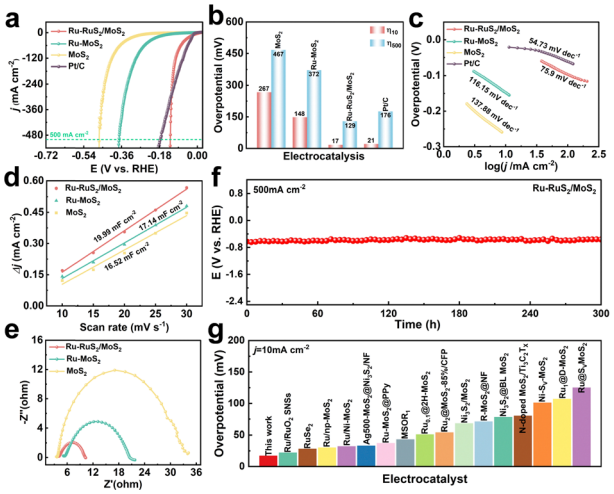

Fig. 3 HER performance in 1 M KOH. (a) LSV curves, (b) overpotentials at current densities of 10 mA cm^{-2} and 500 mA cm^{-2}, and (c) Tafel slopes of MoS_2, Ru–MoS_2, Ru–RuS_2/MoS_2, and commercial Pt/C; (d) electrochemical double-layer capacitance (C_{dl}), (e) electrochemical impedance spectroscopy (EIS); (f) stability testing of the Ru–RuS_2/MoS_2 catalyst; (g) comparison chart of overpotential at a current density of 10 mA cm^{-2}.

In situ techniques were employed to evaluate the adsorption behavior on the catalyst surface. First, electrochemical *in situ* impedance spectroscopy was analyzed using Nyquist plots to assess the conductivity of MoS_2, Ru–MoS_2, and Ru–RuS_2/MoS_2 (Fig. S13, ESI†). The data were fitted using a dual parallel circuit model, where R_2 represents hydrogen adsorption resistance (Fig. S14, ESI†).[20] The R_2 was fitted to the overpotential (Fig. 4a), revealing that Ru–RuS_2/MoS_2 has smaller hydrogen adsorption resistance than Ru-MoS_2, confirming improved hydrogen adsorption and transfer. The Bode plots were applied to further understand the reaction kinetics of HER on MoS_2, Ru–MoS_2, and Ru–RuS_2/MoS_2 (Fig. S15, ESI†). The Bode plot illustrates the variations of phase peak angles (θ) and peak frequency (f_{max}) under different applied voltages, as shown in Fig. 4b. Notably, Ru–RuS_2/MoS_2 exhibits a smaller phase angle (θ) in the low-frequency region and overall higher peak frequencies (f_{max}), indicating that the incorporation of RuS_2 facilitates charge transfer.[21] In order to substantiate the previously discussed conclusions, *in situ* Raman analysis in 1 M KOH verifies that Ru–RuS_2/MoS_2 enhances *H_2O dissociation. In Fig. S16, ESI,† the broad peak observed between 3200 cm^{-1} and 3400 cm^{-1} is attributed to the adsorption of *H_2O.[22] As the potential decreases from 0.20 V to 0 V *vs.* RHE, the intensity of the H_2O adsorption peaks for MoS_2, Ru–MoS_2, and Ru–RuS_2/MoS_2 shows no significant change. However, when the potential is further reduced from 0 V to −0.1 V *vs.* RHE, an obviously weakened adsorption peak of *H_2O is observed for both Ru–MoS_2 and Ru–RuS_2/MoS_2. The relationship between normalized Raman intensity and potential is illustrated in Fig. 4c. It is evident that, compared to MoS_2 and Ru–MoS_2, the *H_2O adsorption peak for Ru–RuS_2/MoS_2 exhibits more pronounced changes during the dissociation phase (from 0 V to −0.1 V *vs.* RHE). This suggests that the incorporation of RuS_2 enhances the dissociation of *H_2O.[23]

To further demonstrate the positive role of the "cross-interfacial electron bridge" (RuS_2) in facilitating electron transfer from Ru to MoS_2, DFT calculations were conducted. The MoS_2 (001), RuS_2 (200), and Ru (101) surfaces were selected as the optimized models for the Ru–RuS_2/MoS_2 heterostructure (Fig. S17, ESI†).[24] The electron transfer behavior was unveiled through differential charge density calculations (Fig. 5a), and the charge density of the Ru–MoS_2 and Ru–RuS_2/MoS_2 models

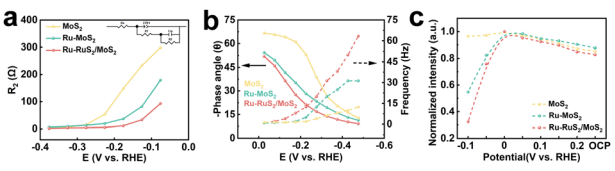

Fig. 4 Electrochemical *in situ* testing (a) Comparison of hydrogen adsorption resistance (R_2) at different voltages; (b) phase peak angles and peak frequencies in the range of −0.026 to −0.476 V (*vs.* RHE); and (c) plot of normalized Raman intensity of the water adsorption peak *versus* potential for MoS_2, Ru–MoS_2, and Ru–RuS_2/MoS_2.

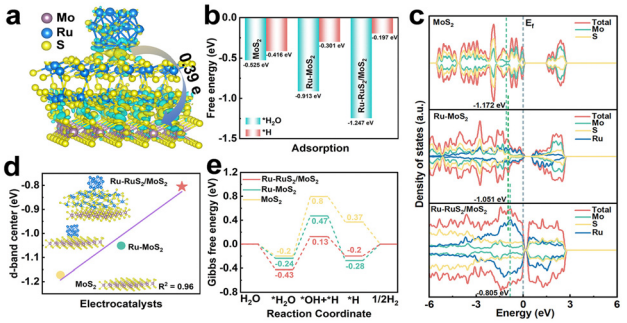

Fig. 5 DFT calculations for MoS_2, Ru–MoS_2, and Ru–RuS_2/MoS_2. (a) Charge density difference plot; (b) free energy of $*H_2O$ and *H adsorption; (c) DOS diagram (density of states diagram); (d) trend chart of d-band center values; (e) HER processes models.

was analyzed using visualized two-dimensional slices (Fig. S19, ESI†). Evidently, RuS_2 induces local charge redistribution, resulting in electron migration from Ru to MoS_2. These electron-deficient Ru sites on the surface can serve as active centers for the appropriate adsorption of various reaction intermediates.[25] Moreover, based on the adsorption structures of $*H_2O$, *OH, and *H on MoS_2, Ru–MoS_2, and Ru–RuS_2/MoS_2 as well as the corresponding adsorption energies (Fig. 5b and Fig. S20–S22, ESI†), the Ru clusters in Ru–RuS_2/MoS_2 are considered as the active sites for the adsorption of *OH, while the adsorption site for *H is the adjacent S atom on RuS_2, which is suitable for HER process. This suggests that Ru–RuS_2/MoS_2 enhances water activation and *H release, improving HER efficiency. Additionally, an analysis of the density of states (DOS) diagrams and d-band center positions for MoS_2, Ru–MoS_2, and Ru–RuS_2/MoS_2 (Fig. 5c and d) was conducted. The construction of the heterostructure reduced the bandgap of the catalyst, with the d-band center of Ru–RuS_2/MoS_2 (−0.805 eV) being closer to the Fermi level (E_f = 0 eV). The d-band centers of the three catalysts demonstrate an exceptional linear fit quality (R^2 = 0.96).[26] A more positive value of the d-band center would reduce the filling of antibonding orbitals, decreasing the interaction between the active sites and the adsorbates. This reduction in antibonding orbital filling in Ru–RuS_2/MoS_2 would yield enhanced σ and π bonds with adsorbed $*H_2O$, thus facilitating the HER process.[27] Furthermore, water dissociation is the rate-determining step in the MoS_2, Ru–MoS_2, and Ru–RuS_2/MoS_2 models (Fig. 5e). The lower water dissociation energy of Ru–RuS_2/MoS_2 indicates that the heterostructure enhances the catalyst's activity and efficiency in HER, as it facilitates a faster supply of the reactive species required for the reaction. According to the hydrogen binding energy (HBE) theory, the Gibbs free energy of *H on Ru–RuS_2/MoS_2 is closer to zero, indicating enhanced HER activity (Fig. 5e).[28]

In conclusion, RuS_2 acts as an electron bridge, improving band alignment, reducing charge transfer resistance, and enabling efficient HER. *In situ* characterization and DFT calculations reveal that the introduction of RuS_2 facilitates the redistribution of localized charge within the catalyst, significantly improving its ability to dissociate $*H_2O$ and promote *H desorption. The Ru–RuS_2/MoS_2 catalyst exhibits an exceptionally low overpotential of merely 17 mV at a current density of 10 mA cm^{-2} for the alkaline HER. Moreover, it demonstrates outstanding stability, maintaining performance for over 300 h at a high current density of 500 mA cm^{-2}. This work highlights an effective interfacial design for improving HER performance.

This work was financially supported by the National Natural Science Foundation of China (No. 2220525, 22105216 and U23A2086), Qingdao Key Technology Research and Industrialization Demonstration Projects (23-1-3-hygg-17-hy), and the Taishan Scholars Program of Shandong Province (No. tstq20221151).

Data availability

The data supporting this article have been included as part of the ESI.†

Conflicts of interest

There are no conflicts to declare.

Notes and references

1 L. Y. Zeng, *et al.*, *Nat. Commun.*, 2022, **13**, 3822.
2 J. W. Zhou, *et al.*, *Angew. Chem.*, 2019, **131**, 3899–3904.
3 J. Deng, *et al.*, *Energy Environ. Sci.*, 2015, **8**, 1594–1601.
4 T. X. Huang, *et al.*, *Nat. Catal.*, 2024, **7**, 646–654.
5 H. Ravichandran, *et al.*, *ACS Nano*, 2023, **17**, 14449–14460.
6 X. Liu, *et al.*, *Small*, 2024, **20**, 2307293.
7 Z. Y. Luo, *et al.*, *Angew. Chem., Int. Ed.*, 2024, **63**, e202405017.
8 T. Wu, *et al.*, *Adv. Sci.*, 2022, **9**, 2202750.
9 R. P. Ma, *et al.*, *Nano Res.*, 2021, **14**, 4321.
10 X. Zhang, *et al.*, *Adv. Sci.*, 2019, **6**, 1900090.
11 B. Müller, *et al.*, *Phys. Chem. Miner.*, 1991, **17**, 716–719.
12 Z. Y. Luo, *et al.*, *Nat. Commun.*, 2020, **11**, 1116.
13 J. W. Zhu, *et al.*, *Angew. Chem., Int. Ed.*, 2021, **60**, 12328–12334.
14 C. H. Zhang, *et al.*, *Nano Res.*, 2023, **16**, 9371–9378.
15 C. A. Zhou, *et al.*, *J. Am. Chem. Soc.*, 2024, **146**, 21453–21465.
16 C. C. Li, *et al.*, *Adv. Energy Mater.*, 2018, **8**, 1801775.
17 S. C. Zhang, *et al.*, *Angew. Chem., Int. Ed.*, 2023, **62**, e202302795.
18 C. Ray, *et al.*, *Chem. Commun.*, 2016, **52**, 6095–6098.
19 C. H. Zhang, *et al.*, *Sci. Bull.*, 2023, **68**, 2042.
20 H. Fan, *et al.*, *Angew. Chem., Int. Ed.*, 2024, e202412080.
21 N. O. Laschuk, *et al.*, *RSC Adv.*, 2021, **11**, 27925–27936.
22 X. Q. Mu, *et al.*, *Angew. Chem., Int. Ed.*, 2024, **63**, e202319618.
23 Q. He, *et al.*, *Adv. Mater.*, 2022, **34**, 2110604.
24 J. H. Wang, *et al.*, *Adv. Funct. Mater.*, 2024, **34**, 2315326.
25 T. J. Qiu, *et al.*, *Nano Energy*, 2019, **58**, 1–10.
26 X. K. Wang, *et al.*, *Nat. Commun.*, 2023, **14**, 7210.
27 J. Wang, *et al.*, *Nat. Commun.*, 2019, **10**, 5692.
28 Z. J. Liang, *et al.*, *Adv. Mater.*, 2024, 2408634.

